Journal of Biomedical Optics

BiomedicalOptics.SPIEDigitalLibrary.org

Multispectral hybrid Cerenkov luminescence tomography based on the finite element SPn method

Haixiao Liu
Xin Yang
Tianming Song
Chengpeng Bao
Liangliang Shi
Zhenhua Hu
Kun Wang
Jie Tian

SPIE.

Multispectral hybrid Cerenkov luminescence tomography based on the finite element SPn method

Haixiao Liu,[a,b,†] Xin Yang,[a,b,†] Tianming Song,[a] Chengpeng Bao,[a] Liangliang Shi,[a,b] Zhenhua Hu,[a,b,*] Kun Wang,[a,b,*] and Jie Tian[a,b,*]
[a]Chinese Academy of Sciences, Key Laboratory of Molecular Imaging, Institute of Automation, Zhongguancun East Road No. 95, Beijing 100190, China
[b]Beijing Key Laboratory of Molecular Imaging, Zhongguancun East Road No. 95, Beijing 100190, China

Abstract. Cerenkov luminescence tomography (CLT) is a promising tool that enables three-dimensional noninvasive *in vivo* detection of radiopharmaceuticals. Conventionally, multispectral information and diffusion theory were introduced to achieve whole-body tomographic reconstruction. However, the diffusion theory inevitably causes systematic error in blue bands of the electromagnetic spectrum due to high-tissue absorption, and CL has a blue-weighted broad spectrum. Therefore, it is challenging to improve the accuracy of CLT. The performance of the *n*-order simplified spherical harmonics approximation (SPn) in different spectra is evaluated, and a multispectral hybrid CLT based on the combination of different SPn models is proposed to handle the Cerenkov photon transport problem in complex media. The *in vivo* xenograft experiment shows that this approach can effectively improve the quality and accuracy of the reconstructed light source. We believe that the new reconstruction method will advance the development of CLT for more *in vivo* imaging applications.
 [DOI: 10.1117/1.JBO.20.8.086007]

Keywords: Cerenkov luminescence tomography; spherical harmonics approximation; multispectral; diffusion theory.
Paper 150168RR received Mar. 16, 2015; accepted for publication Jul. 15, 2015; published online Aug. 13, 2015.

1 Introduction

Cerenkov luminescence (CL) is generated when a charged particle travels with a velocity faster than the speed of light in a medium. It was first used in small animal optical imaging in 2009,[1] and then was proven to have a strong correlation with positron emission computed tomography (PET) and single-photon emission computed tomography (SPECT).[2,3] CL imaging (CLI) can detect the distribution of both positron and electron emitting radioisotopes such as ^{18}F, ^{32}P, and ^{131}I.[4,5] It combines the superiorities of optical imaging and nuclear imaging, so that many clinically approved radiopharmaceuticals can be imaged by optical approaches such as planar imaging and endoscopic imaging.[1,6] Applications in oncology, metabolic pathways, inflammation, and infectious diseases have been studied.[7–10] Human CLI studies, which showed great promise of CLI for clinical translation, have been reported.[11,12]

To overcome the drawback of conventional two-dimensional CLI for lack of depth information, three-dimensional (3-D) CL tomography (CLT) was introduced,[13] which employed the radiation transport equation (RTE) to describe the light propagation in turbid media. As the computational cost of RTE is too high, diffusion theory (DE) was usually applied to solve the approximate problem.[14,15] CL has a blue-weighted broad spectrum (about 300 to 900 nm, peak at 400 nm), and recent studies showed that the third-order spherical harmonics (SP3) method provided a better performance than the DE model did in the case of strong tissue absorption.[16,17] However, all these previous studies did not fully utilize the unique feature of CL to improve the performance of CLT. We hypothesize that by investigating various higher-order spherical harmonic approximations with multispectral data collection, the optimal approximation between scattering and absorption for such a wide spectrum CL can be achieved so that the overall reconstruction accuracy can be further improved with limited sacrifice of computational cost. In this work, we tested the performance of the higher-order spherical harmonics approximation method up to SP7 over seven spectra under the finite element framework and compared the results with the Monte Carlo (MC) method. Based on this comparison, the novel multispectral hybrid CLT (mhCLT) reconstruction method was established. This new approach not only utilizes multispectral information, but also combines SP3 and DE models at different wavelength bands to achieve a more accurate description of *in vivo* CL photon propagation. *In vivo* xenograft experiments were conducted to evaluate this technique, and its feasibility for tumor detection was verified with a PET scan.

2 Methods

2.1 *SPn Model*

The SPn model approximates the RTE by a set of coupled diffusion-like equations with a Laplacian operator. The DE model only retains the first term of the spherical harmonics series, which is essentially the same as the SP1 model. Therefore, it is conceivable that the SP3 model can have a better

*Address all correspondence to: Jie Tian, E-mail: tian@ieee.org; Zhenhua Hu, E-mail: zhenhua.hu@ia.ac.cn; Kun Wang, E-mail: kun.wang@ia.ac.cn

†These authors contributed equally.

1083-3668/2015/$25.00 © 2015 SPIE

performance compared with DE.[16] However, it is still questionable whether the higher order of the SPn model, such as SP5 or SP7, will achieve better approximation of RTE, because the SPn solutions do not converge to exact transport solutions as $N \to \infty$. For each problem, there is an optimal order of SPn that yields the best solution.[18] In addition to that, the higher-order SPn model will also come with a significant increase in computational cost, which is not practical for *in vivo* imaging. Therefore, we investigated the performance of the higher-order spherical harmonics approximation method up to SP7 under the finite element framework to determine which one was the most suitable approach for CLT. Equation (1) includes the steady-state SP3 equations associated with partly reflecting boundary conditions, which are demonstrated as an example for the SPn model. The higher-order SPn equations can be found in the work of Klose and Larsen:[18]

$$\begin{aligned} &-\nabla\cdot\frac{1}{3\mu_{a1}}\nabla\varphi_1+\mu_a\varphi_1=Q+\left(\frac{2}{3}\mu_a\right)\varphi_2\\ &-\nabla\cdot\frac{1}{7\mu_{a3}}\nabla\varphi_2+\left(\frac{4}{9}\mu_a+\frac{5}{9}\mu_{a2}\right)\varphi_2\\ &\quad=-\frac{2}{3}Q+\left(\frac{2}{3}\mu_a\right)\varphi_1, \end{aligned} \tag{1}$$

where $\mu_{ai}=\mu_a+\mu_s(1-g^i)$ $i=1,2,3$, μ_a is the absorption coefficient, μ_s is the scattering coefficient, and g is the anisotropy coefficient. Q is the CL source and φ_i is the i'th order Legendre moments of the radiance.[18]

The boundary conditions are

$$\begin{aligned} &\left(\frac{1}{2}+A_1\right)\varphi_1+\left(\frac{1+B_1}{3\mu_{a1}}\right)n\cdot\nabla\varphi_1\\ &\quad=\left(\frac{1}{8}+C_1\right)\varphi_2+\left(\frac{D_1}{\mu_{a3}}\right)n\cdot\nabla\varphi_2\\ &\left(\frac{7}{24}+A_2\right)\varphi_2+\left(\frac{1+B_2}{7\mu_{a3}}\right)n\cdot\nabla\varphi_2\\ &\quad=\left(\frac{1}{8}+C_2\right)\varphi_1+\left(\frac{D_2}{\mu_{a1}}\right)n\cdot\nabla\varphi_1, \end{aligned} \tag{2}$$

where A_1, B_1, C_1, D_1, A_2, B_2, C_2, and D_2 are the constant coefficients related to the refractive index of the biological tissue. n is the normal vector of the boundary.[18]

The domain of the object is discretized by a tetrahedral grid. The photon flux density and the CL source are approximated with the piecewise linear bases:

$$\begin{cases} \varphi_i(r)=\sum_{k=1}^{N}\varphi_{i,k}v_k(r) & i=1,2\\ Q(r)=\sum_{k=1}^{N}s_kv_k(r) \end{cases}, \tag{3}$$

where $\varphi_{i,k}$ and s_k are the discretized luminescent flux and CL source, respectively, at node k. The bases function $v_k(r)$ is a piecewise linear function. N is the total number of nodes on the entire tetrahedral grid ζ. If we multiply the bases function $v_k(r)$ on both sides of the SP3 equations, integrate on domain Ω, use the Green equation to eliminate the second derivative item, and introduce the boundary conditions, the formulation of Eq. (1) is transferred as follows:

$$J^+=A_{\mathrm{SPn}}s, \tag{4}$$

where A_{SPn} is the system matrix obtained by the SPn method, s is the CL source, and J^+ is the exiting partial luminescent flux.

2.2 *Multispectral Method*

As shown in Sec. 2.1, both the SPn model and the DE model can obtain a system matrix to reveal the relationship between the unknown CL source s and the measurable exiting partial luminescent flux J^+. For a multispectral situation, by taking different spectra exiting J^+ and the CL source spectrum into account, we obtain the mhCLT method from Eq. (4):

$$\begin{bmatrix} \eta(\lambda_1)A_{\mathrm{SPn}_1}(\lambda_1)\\ \cdots\\ \eta(\lambda_k)A_{\mathrm{SPn}_k}(\lambda_k) \end{bmatrix}s=\begin{bmatrix} J^+(\lambda_1)\\ \cdots\\ J^+(\lambda_k) \end{bmatrix}, \tag{5}$$

where $A_{\mathrm{SPn}_i}(\lambda_i)$ stands for the system matrix obtained with the optical properties in spectrum λ_i by the SPn_i model ($n_i=1,3,5,7$). $\eta(\lambda_i)$ is a weighing coefficient determined by the theoretical Cerenkov emission spectrum $\omega(\lambda)$[19] as follows:

$$\eta(\lambda_i)=\frac{\int_{\lambda_i^{\mathrm{low}}}^{\lambda_i^{\mathrm{high}}}\omega(\lambda)\mathrm{d}\lambda}{\int_0^{\infty}\omega(\lambda)\mathrm{d}\lambda}, \tag{6}$$

where $\lambda_i^{\mathrm{high}}$ and λ_i^{low} represent the higher and lower bounds of the i'th filter. When substituting the Cerenkov emission spectrum $\omega(\lambda)$ with $1/\lambda^2$ for approximation, Eq. (6) can be written as follows:

$$\eta(\lambda_i)=\frac{1/\lambda_i^{\mathrm{low}}-1/\lambda_i^{\mathrm{high}}}{1/\lambda_{\min}}. \tag{7}$$

2.3 *Solving the Inverse Problem*

Orthogonal matching pursuit (OMP) is an optimization scheme used for compressed sensing. It can solve the equations of optical tomography through iterations.[20,21] Here, we employed the OMP method to solve Eq. (5).

Equation (5) can be presented as

$$As=J \quad A=\begin{bmatrix} \eta(\lambda_1)A_{\mathrm{SPn}_1}(\lambda_1)\\ \cdots\\ \eta(\lambda_k)A_{\mathrm{SPn}_k}(\lambda_k) \end{bmatrix}, \qquad J=\begin{bmatrix} J^+(\lambda_1)\\ \cdots\\ J^+(\lambda_k) \end{bmatrix}. \tag{8}$$

The inverse model of mhCLT can be approximately regarded as a basis pursuit problem:

$$\begin{cases} \min\|s\|_1\\ \text{s.t. } As=J \end{cases}. \tag{9}$$

We set the supporting index set I to represent the vertex index whose light source is not zero, and the OMP starts with an empty supporting index set. Then

$$I_k=I_{k-1}\cup\{p{:}c_k(p)>t_k\}, \tag{10}$$

where $c_k=A^Tr_{k-1}$ and $t_k=\alpha\|c_k\|_\infty\alpha\in(0,1)$. For the k'th iteration, the residual vector r_{k-1} is as follows:

$$r_{k-1} = J - As_{k-1}. \tag{11}$$

By introducing the supporting index set I_k, Eq. (8) can be simplified as

$$A_{I_k} s_{I_k} = J. \tag{12}$$

Finally, the reconstructed source s can be expressed as the least-squares solution of the problem:

$$A_{I_k}^T A_{I_k} s_{I_k} = A_{I_k}^T J. \tag{13}$$

The stop condition of the iteration is defined as the number of I_k that exceeds the estimated threshold.

3 Results

3.1 *Forward Simulation*

A digital mouse was used to assess the performance of all the SPn models. The light source was set to be 1.8 mm beneath the skin surface. We discretized the phantom with 8254 nodes and 41,922 tetrahedrons, as shown in Fig. 1(a). All the forward models, including DE(SP1), SP3, SP5, and SP7, were applied on the finite element grid, and the MC method was considered to be the gold standard[22] to evaluate which model was better in each spectrum (550, 600, 650, 700, 736, 800, and 855 nm). The MC method was conducted by MOSE v2.1. The results of the MC method are shown in Fig. 1(b). Two examples of the simulation for 600 and 800 nm are shown in Fig. 1(c). Compared with MC, DE showed a relatively poorer skin surface photon flux in 600 nm, whereas in 800 nm, the flux of DE appears to be much better. To achieve a quantitative assessment, the cosine similarity was adopted to measure the similarity of the surface photoflux between MC and other forward models:

Table 1 The optical properties for 650 nm.

Organ	μ_a (mm^{-1})	μ_s (mm^{-1})	g
Muscle	0.12	15.58	0.97
Lungs	0.26	31.56	0.93
Heart	0.08	10.07	0.90
Bone	0.08	37.27	0.93
Liver	0.47	10.00	0.93
Kidneys	0.09	23.59	0.90

$$\rho = \frac{J_1^+ \cdot J_2^+}{\|J_1^+\|_2 \|J_2^+\|_2} = \frac{\sum_{k=1}^{M} j_{1,k} j_{2,k}}{\sqrt{\sum_{k=1}^{M} j_{1,k}^2} \sqrt{\sum_{k=1}^{M} j_{2,k}^2}}, \tag{14}$$

where M is the number of nodes on the surface, and $j_{i,k}$ is the k'th element of vector J_i^+.

The optical properties μ_a and μ_s were calculated based on the work of Alexandrakis et al.[23] As the anisotropy coefficient g varies slightly over the spectra, we assumed it was a constant.[24] As an illustration, the optical properties used for 650 nm are listed in Table 1. The results for different models are shown in Fig. 2. The cosine similarity results are shown in Table 2.

The results showed that none of the models reached 50% cosine similarity at 550 nm. This was probably because of the high-absorption effect of the soft tissue. However, when the wavelength reached 600 nm and above, the cosine similarity improved dramatically (Table 2). The SP3 model was more accurate than the DE model over all spectra. The accuracies of the SP5 model and SP7 model were almost the same as

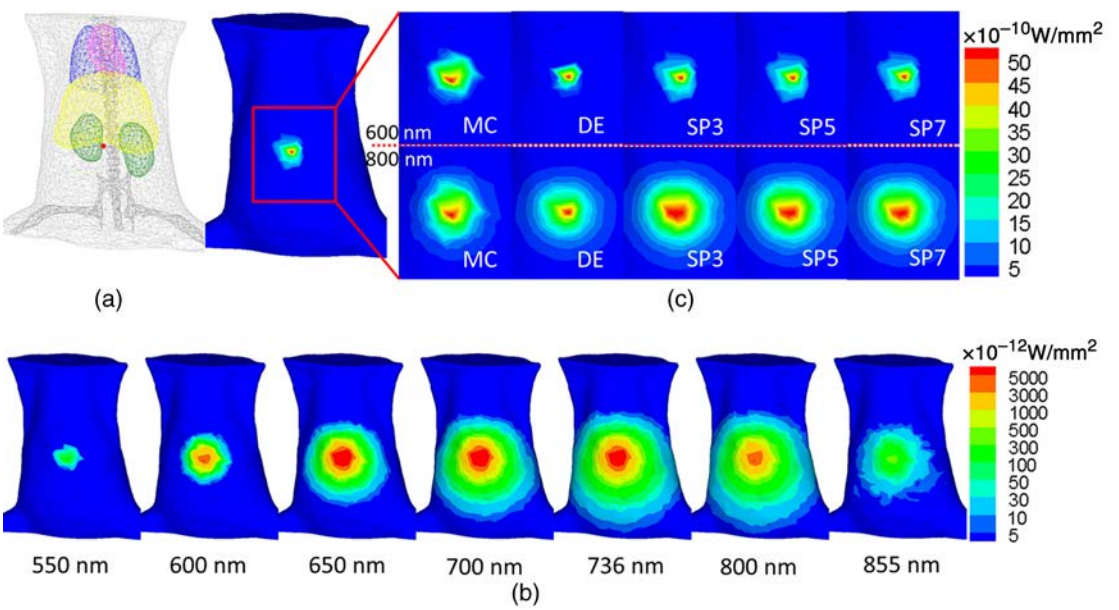

Fig. 1 The results of the forward simulation: (a) the digital mouse used to simulate the forward model. Heart (read), lungs (blue), liver (yellow), kidneys (green), and bone (black) were segmented. The rest was set to be muscle. The red point was the light source. There were 8254 nodes and 41,922 tetrahedrons in total; (b) the simulation result of different spectra (550 to 855 nm) using the MC method; and (c) two examples of the simulated optical flux in 600 and 800 nm using different forward models.

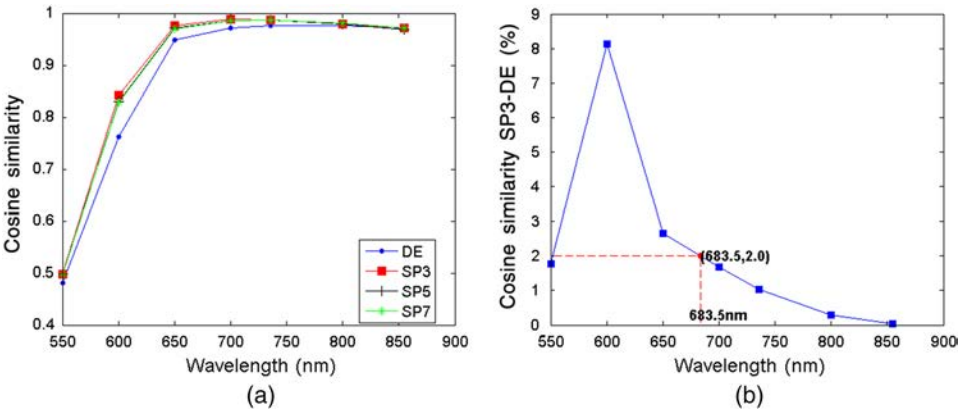

Fig. 2 The quantitative comparison between different SPn models: (a) The cosine similarity of different forward models, which was used to judge the accuracy of these models in the function of the spectrum (600 to 855 nm); and (b) the difference between SP3 cosine similarity and DE cosine similarity. Two percent was considered to be the threshold.

Table 2 The cosine similarity between the SPn model results and the MC model results.

%	550 nm	600 nm	650 nm	700 nm	736 nm	800 nm	855 nm
SP1	48.10	76.23	95.05	97.26	97.76	97.77	97.29
SP3	49.87	84.36	97.71	98.94	98.80	98.06	97.34
SP5	49.77	83.07	97.22	98.72	98.80	98.05	97.10
SP7	49.67	82.96	97.16	98.71	98.84	98.24	97.34

that of the SP3 model. The major difference was between the DE and SP3 models [Fig. 2(a)], which varied from 8.13% to 0.05% and from 600 to 855 nm. This proved that for a shorter wavelength and higher absorption situation, SP3 was more accurate than DE,[16] but for a longer wavelength and lower absorption situation, the difference was almost negligible. When solving the inverse problem, which is the calculation of a light source from the surface CL flux [Eqs. (8)–(13)], the employed mathematical model should be as accurate as possible, because the inaccuracy of a forward model may lead to a significant reconstruction error due to the ill-posed problem of Eq. (8).[25] In other words, a small change of J would introduce a significant variation of s in Eq. (8). Meanwhile, the mathematical model should also consider the computational cost, because if the reconstruction time is too long, it would be very unpractical for real biomedical applications. Therefore, there is a balance between reconstruction accuracy and computational time.

In this study, a 2% difference between these two models was set as the threshold. The dividing line between the SP3 model and the DE model was 683.5 nm [Fig. 2(b)]. Thus, if the wavelength was below 683.5 nm, the SP3 model was used to describe the photon transmission, whereas for a wavelength above 683.5 nm, the DE model was employed. Mathematically speaking, it will have a threefold increase of the computational cost for adopting SP3 instead of DE,[18] but the difference of the computational time is not obvious due to the fast development of the computing power in computers, and we only employed SP3 for a partial CL spectrum to further save the time. SP5 and SP7 models were discarded because of the high computational cost with no significant benefit in accuracy.

3.2 *Simulated Comparison Between mhCLT and SP3*

The mhCLT was compared with the conventional single wavelength SP3 method[16] in accuracy using a simulation study. Two CL sources were set inside the liver of a digital mouse [Fig. 3(a)], and the mouse was discretized with 4309 nodes and 21,979 tetrahedrons. Three spectra (650, 700, and 736 nm) were employed to obtain system matrix A [Eq. (8)] of the mhCLT method. Based on our previous findings, for 650 nm (wavelength below 683.5 nm), the SP3 model was applied. For 700 and 736 nm (wavelength above 683.5 nm), the DE model was used. After that, the OMP iterative algorithm was used to solve Eq. (8) and calculate the distribution of the two CL sources. As a comparison, the conventional SP3 reconstruction was conducted on the 700-nm spectrum. The reconstructed results of both methods are shown in Fig. 3 and Table 3, which revealed that the mhCLT achieved accurate reconstruction of both sources, whereas SP3 could only reconstruct one CL source accurately (Source 1), but lost the accuracy of the other (Source 2).

3.3 *In Vivo mhCLT*

All animals utilized in the experiment were purchased from the Department of Laboratory Animal Science, Peking University

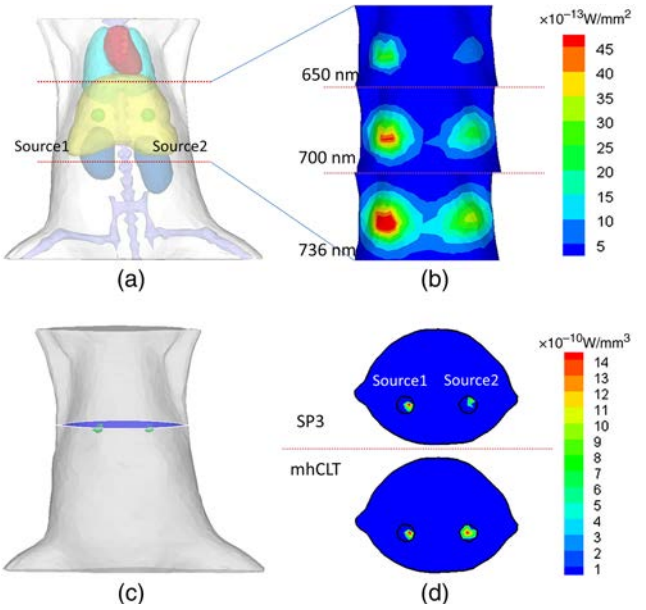

Fig. 3 The simulated comparison between mhCLT and SP3 for CL source reconstruction: (a) the digital mouse used in the simulation. Lungs (light blue), heart (red), liver (yellow), kidneys (blue), and bone (purple) were segmented. The two green spots inside the liver are the CL sources; (b) the surface CL fluxes of different spectra generated from the dual light source in (a); (c) the axial slice location used in (d) for comparison; and (d) the reconstruction results of different methods. Top: the result of the SP3 method, and bottom: the result of the mhCLT method. The black circles are the real light sources.

Health Science Centre. Animal experimentation was conducted under approved research protocols of the Institutional Animal Care and Use Committee, Chinese Academy of Sciences.

A healthy, female nude mouse was injected with 836 uCi ^{18}F-FDG through the tail vein and anesthetized with 2% isoflurane during the experiment. After 40 min, when the circulation carried the FDG to the bladder, the mouse was photographed by an Andor EMCCD camera to obtain the CL image and was then taken to do a CT scan using a micro-CT system to get the 3-D volume data. The exposure time was 5 min, and the gain value was 800. Three optical filters (Semrock FF01-650/100-25, FF01-736/128-25, and FF01-855/210-25) were applied for multispectral image acquisition. After that, the CL images and CT data were processed following the flowchart in Fig. 4.

First, the CT data were segmented into different organs. All organs were recombined and discretized into a volumetric mesh which contained 4628 vertices and 22,827 tetrahedral elements. Second, the CL images of different spectra were mapped on the volumetric mesh according to the registration markers to get the surface energy distribution. The mhCLT method was used to reconstruct the CL source. As a comparison, we also tested the DE multispectral CLT (msCLT) described in Ref. 19, and the results are shown in Table 4 and Fig. 5. The distance error of mhCLT versus msCLT is 1.1 mm versus 2.0 mm. The real source was approximately set to be the center of the bladder (according to the CT data). The reconstructed source position was set to be the coordinates of the vertex which has the maximum energy intensity. As shown in Fig. 5, the source obtained by msCLT was partially outside the bladder [Figs. 5(b) and 5(e)], but the source obtained by mhCLT was inside the bladder [Figs. 5(a) and 5(d)].

3.4 *In Vivo Imaging of a Xenograft Using mhCLT*

4T1 breast cancer cells were injected into a BALB/c nude mouse to establish the tumor mouse model. Two weeks after the injection, the multispectral optical [Figs. 6(a)–6(c)] and CT data were acquired and processed using the same process as Fig. 4. Figure 6(d) demonstrates the difference between the filtered and no-filtering optical data. The 3-D reconstruction of mhCLT was then compared with PET images. Note that the mouse was moved from the CLT system to the PET system. Although the body posture for the two imaging devices was different, the tumor lesion reconstruction could still be reasonably compared [Figs. 6(h)–6(m)]. The PET showed that the ^{18}F-FDG uptake in the tumor was not homogeneous, but was concentrated in the peripheral areas deeper inside the body [Figs. 6(h)–6(j)]. This phenomenon was commonly observed because tumor cell necrosis was usually found in the center area of the tumor lesion. The mhCLT successfully reconstructed the ^{18}F-FDG uptake area that was close to the body surface, but it failed to reconstruct the uptake area that was deeper inside the tumor lesion [Figs. 6(e), 6(k), 6(l), and 6(m)].

4 Discussion

This study demonstrated a new approach which combined the multispectral information and the multiorder SPn models to further improve the reconstruction accuracy for CLT. The performances of different SPn models on different spectra of CL were compared with the MC model through simulation. The results showed that although SP3, SP5, and SP7 indeed improved the accuracy compared with the conventional DE model, the difference between these three models was not significant.

To balance the accuracy and the computational cost based on the simulation results, our new mhCLT technique employed SP3 and DE models for short and long wavelength fluxes and utilized this hybrid information to solve the Cerenkov photon transport problems in complex media. Unlike the conventional optical tomographic methods for bioluminescence and

Table 3 The reconstructed energy center of the single spectrum SP3 and mhCLT.

		Source 1 (left) (mm)		Source 2 (right) (mm)	
		Position	Error	Position	Error
Real light source		(6.80, 3.80, 4.80)	—	(−3.20, 3.80, 4.80)	—
Reconstructed light source	SP3	(7.08, 3.73, 4.49)	0.42	(−3.30, 4.61, 4.50)	0.87
	mhCLT	(6.65, 3.79, 5.05)	0.29	(−3.02, 3.82, 4.48)	0.37

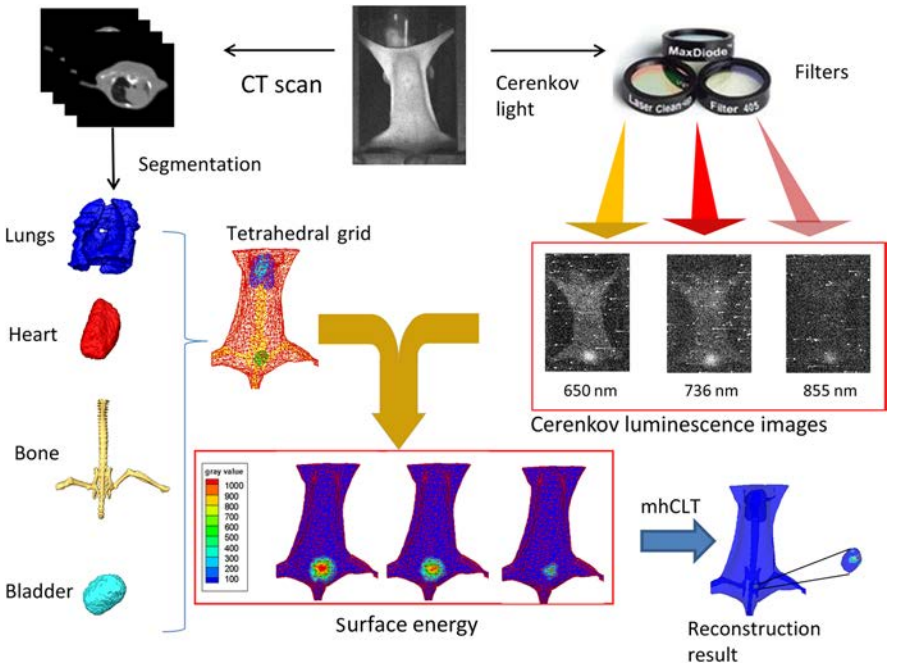

Fig. 4 The data preprocessing of the mhCLT.

Table 4 The reconstructed energy center of the mhCLT and msCLT.

Method		Position (mm)	Distance (mm)
Real source		1.49, 7.92, −32.50	—
Reconstructed source	mhCLT	1.74, 6.87, −32.29	1.10
	msCLT	1.95, 6.37, −31.34	1.99

fluorescence tomography, this method made full use of the wide spectrum feature of CL. Unlike the other methods for CLT, it also avoided the unnecessary computations for higher-order spherical harmonics approximation.

To validate the superiority in accuracy for mhCLT, we compared it with the conventional SP3 method through a dual-source simulation experiment, and the results proved that the new approach could offer better accuracy for multisource reconstruction. We also compared mhCLT with conventional msCLT for *in vivo* mouse imaging. The quantitative analysis proved that the mhCLT provided better accuracy for ^{18}F-FDG concentration in the bladder. Although both methods adopted multispectral information, the DE model in msCLT caused systematic errors, especially for a short wavelength flux, and led to a larger position deviation between the real source and the reconstructed source. The mhCLT improved the accuracy by combining both DE and SP3 models. To further investigate the feasibility of mhCLT, we compared it with PET for *in vivo* tumor mouse imaging. The results showed that the reconstructed ^{18}F-FDG uptake region from mhCLT was not geometrical in

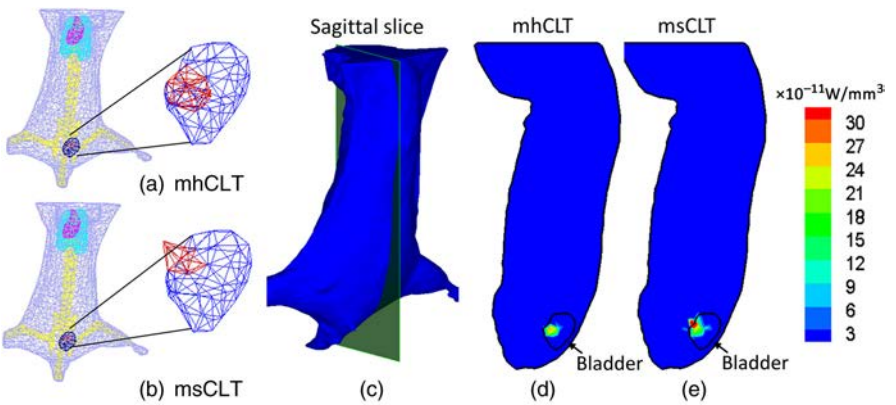

Fig. 5 CLT reconstruction results of the mouse bladder: (a) and (b) three-dimensional (3-D) view of the reconstruction results of the mhCLT and msCLT separately. Lungs (blue), heart (pink), bone (yellow), and bladder (blue) were segmented from the CT data. The red part is the reconstructed light source; (c) illustration of the location of the two-dimensional (2-D) slice used in (d) and (e); and (d) and (e) the 2-D view (sagittal) of the light source reconstruction obtained by mhCLT and msCLT, respectively.

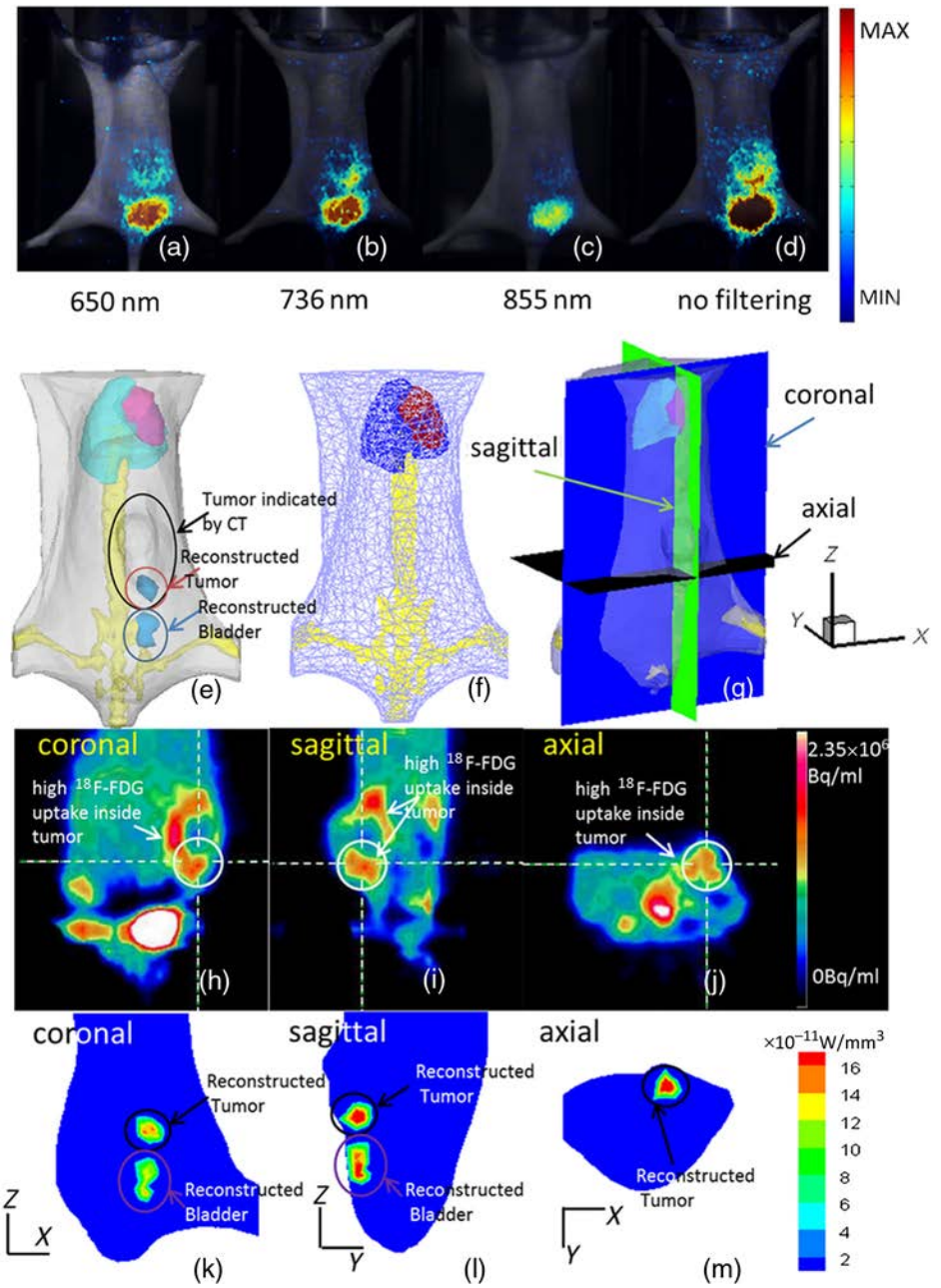

Fig. 6 The comparison between mhCLT and positron emission computed tomography (PET) for *in vivo* tumor detection: (a)–(c) the 2-D CL images over different wavelengths acquired for the 3-D tomographic reconstruction; (d) the 2-D CL image of the same subject without filtering; (e) the contour of the tumor lesion detected by CT (black circle), the mhCLT reconstructed tumor lesion (red circle), and bladder area (blue circle); (f) the volumetric mesh of the mouse, which shows the heart (red), lungs (blue), and bone (yellow); (g) the illustration of the coronal, sagittal, and axial planes used for PET and mhCLT comparison; (h)–(j) the results of the PET scan. The green circles indicate the regions that were also seen in mhCLT; and (k)–(m) the results of mhCLT. The black circles indicate the regions that were also seen in PET.

the center of the tumor lesion as indicated by CT [Fig. 6(e)]. However, it showed great consistency with PET. Both imaging modalities indicated that the high glycometabolism area was in the tumor periphery instead of the tumor center, which was likely caused by tumor cell necrosis. We also found that compared with PET, mhCLT was not able to reconstruct the whole ^{18}F-FDG uptake region inside the tumor. This was probably because the region was too deep inside the body, which caused an insufficient CL flux to be detected by the imaging system. This implies that no matter how accurate the mathematical model is, the reconstruction of the CL source still relies on the sensitivity of the imaging system in the detection of the CL flux on the body surface.

5 Conclusion

By combining the SP3 and DE models with multispectral information, the mhCLT method can provide an accurate

reconstruction for *in vivo* CLT imaging. We believe this new method will further benefit various preclinical applications of CLT and facilitate its clinical translation in the future.

Acknowledgments

This paper is supported by the National Basic Research Program of China (973 Program) under Grants 2011CB707700 and 2015CB755500, and the National Natural Science Foundation of China under Grant Nos. 81227901, 61231004, 61401462, and 61302024.

References

1. R. Robertson et al., "Optical imaging of Cerenkov light generation from positron emitting radiotracers," *Phys. Med. Biol.* **54**(16), N355–N365 (2009).
2. A. Ruggiero et al., "Cerenkov luminescence imaging of medical isotopes," *J. Nucl. Med.* **51**, 1123–1130 (2010).
3. Z. Hu et al., "Experimental Cerenkov luminescence tomography of the mouse model with SPECT imaging validation," *Opt. Express* **18**(24), 24441–24450 (2010).
4. J. C. Park et al., "Luminescence imaging using radionuclides: a potential application in molecular imaging," *Nucl. Med. Biol.* **38**, 321–329 (2011).
5. Z. Hu et al., "Three-dimensional noninvasive monitoring iodine-131 uptake in the thyroid using a modified Cerenkov luminescence tomography approach," *PloS One* **7**(5), e37623 (2012).
6. C. Carpenter et al., "Cerenkov luminescence endoscopy: improved molecular sensitivity with β-emitting radiotracers," *J. Nucl. Med.* **55**, 1905–1909 (2014).
7. D. L. J. Thorek et al., "Quantitative imaging of disease signatures through radioactive decay signal conversion," *Nat. Med.* **19**(10), 1345–1350 (2013).
8. A. Natarajan et al., "Evaluation of 89Zr-rituximab tracer by Cerenkov luminescence imaging and correlation with PET in a humanized transgenic mouse model to image NHL," *Mol. Imaging Biol.* **15**, 468Y475 (2013).
9. Y. Xu et al., "Proof-of-concept study of monitoring cancer drug therapy with Cerenkov luminescence imaging," *J. Nucl. Med.* **53**, 312–317 (2012).
10. Z. Hu et al., "Cerenkov luminescence tomography of aminopeptidase N (APN/CD13) expression in mice bearing HT1080 tumors," *Mol. Imaging* **12**(3), 173–181 (2013).
11. A. E. Spinelli et al., "First human Cerenkography," *J. Biomed. Opt.* **18**(2), 020502 (2013).
12. D. Thorek, C. Riedland, and J. Grimm, "Clinical Cerenkov luminescence imaging of (18)F-FDG," *J. Nucl. Med.* **55**(1), 95–98 (2014).
13. C. Li, G. S. Mitchell, and S. R. Cherry, "Cerenkov luminescence tomography for small-animal imaging," *Opt. Lett.* **35**(7), 1109–1111 (2010).
14. M. Schweiger et al., "The finite element method for the propagation of light in scattering media: boundary and source conditions," *Med. Phys.* **22**, 1779–1792 (1995).
15. A. D. Klose, V. Ntziachristos, and A. H. Hielscher, "The inverse source problem based on the radiative transfer equation in optical molecular imaging," *J. Comput. Phys.* **202**, 323–345 (2005).
16. J. Zhong et al., "Whole-body Cerenkov luminescence tomography with the finite element SP3 method," *Ann. Biomed. Eng.* **39**(6), 1728–1735 (2011).
17. K. Liu et al., "Evaluation of the simplified spherical harmonics approximation in bioluminescence tomography through heterogeneous mouse models," *Opt. Express* **18**(20), 20988–21002 (2010).
18. A. D. Klose and E. W. Larsen, "Light transport in biological tissue based on the simplified spherical harmonics equations," *J. Comput. Phys.* **220**, 441–470 (2006).
19. A. E. Spinelli et al., "Multispectral Cerenkov luminescence tomography for small animal optical imaging," *Opt. Express* **19**(13), 12605–12618 (2011).
20. D. Han et al., "Efficient reconstruction method for L1 regularization in fluorescence molecular tomography," *Appl. Opt.* **49**(36), 6930–6937 (2010).
21. J. Tropp and A. Gilbert, "Signal recovery from random measurements via orthogonal matching pursuit," *IEEE. Trans. Inf. Theory* **53**, 4655–4666 (2007).
22. H. Li et al., "A mouse optical simulation environment (MOSE) to investigate bioluminescent phenomena in the living mouse with the Monte Carlo method," *Acad. Radiol.* **11**, 1029–1038 (2004).
23. G. Alexandrakis, F. R. Rannou, and A. F. Chatziioannou, "Tomographic bioluminescence imaging by use of a combined optical-PET (OPET) system: a computer simulation feasibility study," *Phys. Med. Biol.* **50**, 4225–4241 (2005).
24. W. Cheong, S. A. Prahl, and A. J. Welch, "A review of the optical properties of biological tissues," *IEEE J. Quantum Electron.* **26**(12), 2166–2185 (1990).
25. K. Ames and B. Straughan, *Non-Standard and Improperly Posed Problems*, Academic Press, San Diego (1997).

Haixiao Liu is a doctoral student in the Key Laboratory of Molecular Imaging, Chinese Academy of Sciences, Beijing, China. He received his BS degree from Harbin Engineering University in 2011. His research interests are mainly focused on the reconstruction methods and applications of Cerenkov luminescence tomography.

Xin Yang is an IEEE member, professor in the Key Laboratory of Molecular Imaging, Institute of Automation, Chinese Academy of Sciences (CAS). She obtained her PhD in Tianjin University in 2000. Her research interests are medical image processing and analysis, pattern recognition. She has published more than 50 papers in academic journals and international conferences.

Zhenhua Hu is an associate professor in the Key Laboratory of Molecular Imaging, Institute of Automation, CAS. She obtained her PhD in the Intelligent Information Processing Center, Xidian University in 2012. Her research interests are the application, instrumentation and reconstruction method of Cerenkov luminescence.

Kun Wang is an associate professor in the Key Laboratory of Molecular Imaging, Institute of Automation, CAS. He obtained his PhD in the Institute of Cellular Medicine, Newcastle University, United Kingdom in 2011. Then, he joined in the CAS. He endeavors to develop new optical and photoacoustic imaging techniques and translate them for clinical applications. His work includes both optical imaging model development and innovation of various imaging systems.

Jie Tian is an IEEE member, IAMBE fellow, SPIE fellow, AIMBE fellow, IAPR fellow, professor in the Key Laboratory of Molecular Imaging, Institute of Automation, CAS. He received his PhD in artificial intelligence from the Institute of Automation, CAS in 1993. His research interests are medical image processing and analysis, pattern recognition, biometics, etc. He has published more than 200 papers in peer-reviewed journals including PANS and IEEE transactions.

Biographies for the other authors are not available.